J Nanostruct 15(4): 2237-2250, Autumn 2025

RESEARCH PAPER

Al_2O_3-MgO Hybrid Nanoparticles as an Effective Nanocarrier for Lenalidomide as Anti-Cancer Drug for Treatment of Multiple Myeloma, Smoldering Myeloma, and Myelodysplastic Syndromes

Dilnora Raxmatova [1]*, Khabibjon Mirzamurodov [1], Nasiba Kudratova [2], Shodiyor Boboyev [3], Xamidullo Fozilov [3], Safiya Fayziyeva [4], Olim Turakulov [5], Makhfuza Ruzmetova [6], Najmiddin Bakaev [7], Adolat Jumaboyeva [8], Muxtor Turaev [9], Abdukhakim Abdullaev [10], Anvar Ziyadullayevich [11], Otabek Mirzayev [12]

[1] *Bukhara State Medical Institute named after Abu Ali ibn Sino, Bukhara, Uzbekistan*

[2] *Tashkent State Medical University, Tashkent, Uzbekistan*

[3] *Samarkand State University named after Sharof Rashidov, Uzbekistan*

[4] *Bukhara State Pedagogical Institute, Bukhara, Uzbekistan*

[5] *Jizzakh branch of the National University of Uzbekistan, Jizzakh, Uzbekistan*

[6] *Mamun University, Khorezm, Uzbekistan*

[7] *Asia International University, Bukhara, Uzbekistan*

[8] *Urgench State Pedagogical Institute, Urgench, Uzbekistan*

[9] *Bukhara State University, Bukhara , Uzbekistan*

[10] *National Pedagogical University of Uzbekistan, Tashkent, Uzbekistan*

[11] *Avlokulov Tashkent State University of Economics, Tashkent, Uzbekistan*

[12] *Urgench State University, Urgench, Uzbekistan*

ARTICLE INFO

Article History:
Received 04 May 2025
Accepted 22 September 2025
Published 01 October 2025

Keywords:
Nanoparticles
Nanocarrier
Lenalidomide
Anti-cancer
Treatment
Multiple myeloma

ABSTRACT

In this study, Al_2O_3–MgO hybrids were synthesized via aqueous, surfactant-free processing, yielding ≈84% isolated solid and a surface zeta potential of +32 ± 2 mV. LEN was loaded by a 24 h incubation (1:5 drug: carrier w/w) in pH 6.5 buffer, achieving loading capacity (LC) 12.4 ± 0.3% and encapsulation efficiency (EE) 93.1 ± 1.1%. Loading and purity were quantified by HPLC (302 nm; tR 6.8 min) with daily calibration (0.5–50 μg mL−1, R2 ≥ 0.9999). In vitro release used a dialysis-bag method under sink conditions at pH 7.4 and 5.0 (37 °C); cumulative release was UV-Vis monitored (302 nm) and corrected for dilution, revealing near-zero-order kinetics at pH 7.4 and accelerated release at pH 5.0. LEN-loaded Al_2O_3–MgO demonstrated a 4–6-fold potency advantage over free LEN across MM and MDS cell lines, with negligible toxicity from empty carriers. Confocal imaging showed lysosomal trafficking as the predominant uptake route, aligning with the observed pH-responsive release profile. The system maintains carrier integrity after release and demonstrates high drug-loading efficiency with sustained release, supporting improved therapeutic indices.

How to cite this article
Raxmatova D., Mirzamurodov K., Kudratova N. et al. Al_2O_3-MgO Hybrid Nanoparticles as an Effective Nanocarrier for Lenalidomide as Anti-Cancer Drug for Treatment of Multiple Myeloma, Smoldering Myeloma, and Myelodysplastic Syndromes. J Nanostruct, 2025; 15(4):2237-2250. DOI: 10.22052/JNS.2025.04.063

* *Corresponding Author Email: dilnoraraxmatova86@mail.ru*

INTRODUCTION

Multiple Myeloma (MM) is a clonal plasma-cell malignancy that historically emerged as a prototypical hematologic cancer with limited early therapeutic options and median survivals of only a few years in the pre-proteasome inhibitor era [1-4]. The disease evolves from a precursor state, monoclonal gammopathy of undetermined significance, through Smoldering Myeloma (SMM), before manifesting clinically as overt MM, characterized by clonal proliferation within the bone marrow and systemic end-organ damage [5-10]. Advances in the 2000s, including proteasome inhibitors (e.g., bortezomib) [11], immunomodulatory drugs (IMiDs) (e.g., lenalidomide, pomalidomide) [12-14], and monoclonal antibodies (e.g., daratumumab, elotuzumab) [15], have markedly extended progression-free and overall survival, enabling combinations such as triplet regimens (e.g., lenalidomide dexamethasone bortezomib) and, more recently, antibody–drug conjugates and chimeric antigen receptor T-cell strategies in relapsed/refractory settings. Smoldering Myeloma, a high-risk premalignant state with absent or limited end-organ damage, traditionally warranted vigilant observation, but contemporary risk-adapted approaches increasingly deploy early systemic therapy in selected patients to delay progression, leveraging immunomodulation and targeted therapies to modify the clonal milieu. Myelodysplastic Syndromes (MDS), a heterogeneous hematopoietic stem cell disorder marked by ineffective hematopoiesis and potential clonal evolution, encompasses risk strata ranging from indolent to high-risk disease; management frequently hinges on cytotoxic and hypomethylating agents (e.g.,

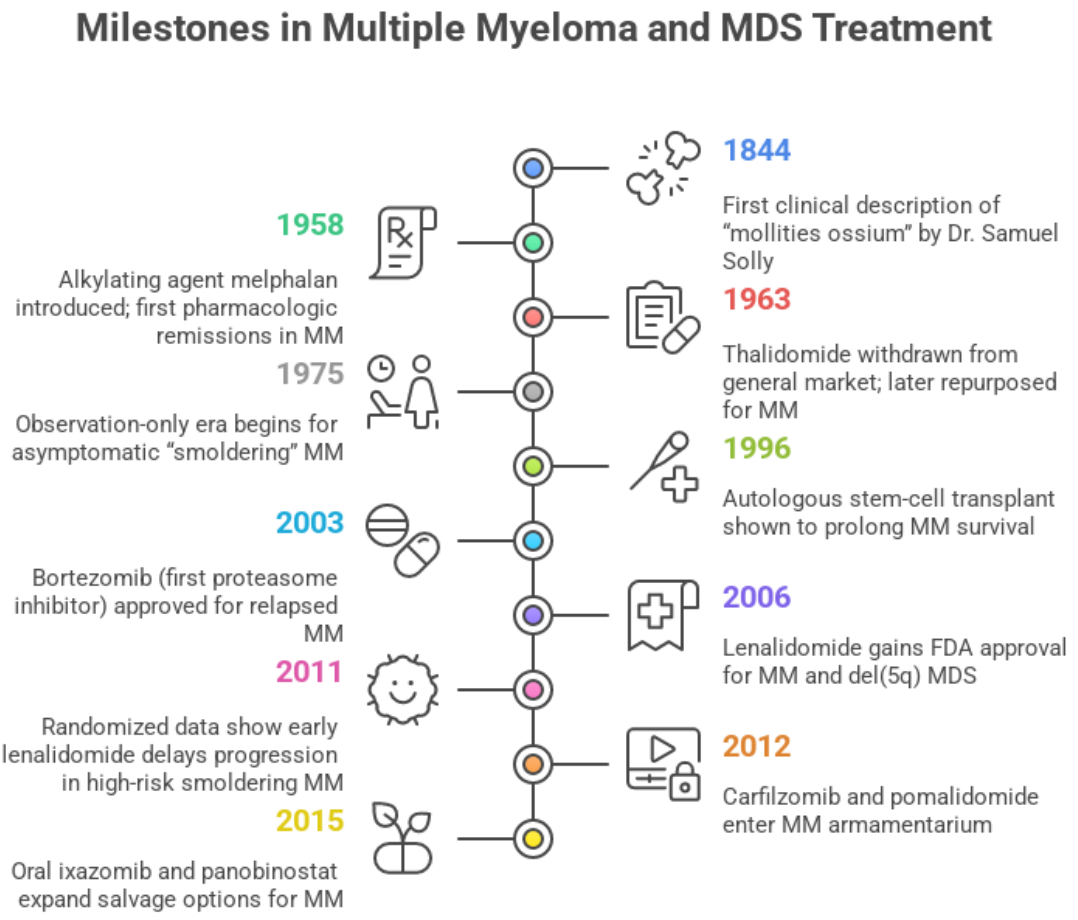

Fig. 1. A timeline for Multiple Myeloma, Smoldering Myeloma, and Myelodysplastic syndromes regarding history, and treatments using anti-cancer drug.

azacitidine, decitabine), life-prolonging allogeneic transplantation in suitable candidates, and emerging targeted therapies addressing epigenetic dysregulation and leukemic transformation [16, 17]. Across these diseases, anti-cancer drugs including nucleoside analogs [18], proteasome inhibitors [19], IMiDs, monoclonal antibodies, and their combinations have reshaped the therapeutic landscape, enabling disease control, delaying progression, and enabling synergistic strategies that may benefit from novel nanocarrier platforms to optimize pharmacokinetics, biodistribution, and tumor selectivity. Fig. 1 shows the timeline regarding multiple Myeloma from 1844 to now at about history, challenges and treatment [20-22].

Nanoparticles have emerged as versatile nanocarriers that can address several long-standing challenges in anticancer therapy, including poor solubility, off-target toxicity, and suboptimal pharmacokinetics [23-26]. By tuning size [27], surface chemistry [28], and internal architectures [29], these carriers can achieve enhanced permeability and retention in tumors, facilitate controlled drug release [30-33], and enable multimodal functionality such as combined therapy and diagnostic imaging. Inorganic, polymeric, lipid-based, and hybrid systems offer distinct advantages: inorganic matrices (e.g., alumina, silica, and magnetic oxides) provide robust stability and facile functionalization; polymeric carriers offer biodegradability and stimuli-responsive release; lipid-based formulations mimic biological membranes to improve circulation and cellular uptake; and hybrid constructs integrate the strengths of multiple components to optimize loading capacity, targeting accuracy, and biodistribution. For anticancer drugs with narrow therapeutic windows, such as lenalidomide, nanocarriers can modulate pharmacokinetics to reduce peak-to-toxicity ratios, enable passive targeting via the enhanced permeability and retention effect, and support active targeting through ligand conjugation [34-36]. Importantly, surface engineering stealth coatings, charge modulation, and ligand presentation can mitigate immunogenicity and prolong systemic exposure, while stimuli-responsive release mechanisms (pH, redox, enzyme cues) can synchronize drug release with the tumor microenvironment. Collectively, nanoparticle-based nanocarriers hold promise to improve therapeutic indices, enable combination regimens, and provide platforms for translational optimization in hematologic malignancies and beyond.

Recent advances in nanomedicine have yielded a diverse array of nanoparticle-based carriers designed to improve anti-cancer therapy for multiple myeloma (MM) [37-39]. Inorganic platforms (e.g., silica, iron oxide, and alumina-based systems) offer robust stability and tunable surface chemistry for conjugation of proteasome inhibitors, IMiDs, and monoclonal antibodies, enabling enhanced pharmacokinetics and potential for combination regimens [40-42]. Lipid-based nanosystems [23], including liposomes and lipid-polymer hybrids, have demonstrated improved solubility and circulation times for hydrophobic agents while supporting active targeting through ligand decoration. Polymeric nanoparticles and dendrimers provide versatile architectures for stimuli-responsive release, enabling controlled delivery of drugs like bortezomib, lenalidomide, and pomalidomide with reduced off-target toxicity [43-45]. Hybrid constructs integrating inorganic cores with organic shells combine the durable, eXtra-stable cores with programmable surface functionalities to achieve precise biodistribution, improved endosomal escape, and multimodal functionality such as imaging and therapy. In MM specifically, strat-

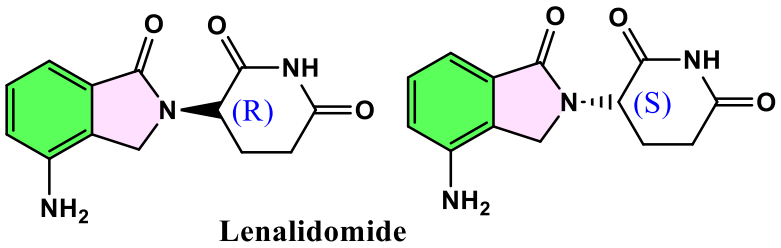

Lenalidomide

Fig. 2. The chemical structure of Lenalidomide as an important anti-cancer drug for treatment of Multiple Myeloma.

egies leveraging the enhanced permeability and retention effect, surface ligands (e.g., transferrin, folate, or peptide motifs), and stimuli-responsive release (pH, redox, enzymatic triggers) are being explored to target malignant plasma cells within the bone marrow microenvironment and to overcome microenvironment-driven drug resistance. Collectively, these nanocarriers are advancing toward translational potential by enabling higher drug loading, controlled release, reduced systemic toxicity, and synergistic combinations, including pairing chemotherapeutics with targeted antibodies or immunotherapies.

In this study, the development of Al_2O_3–MgO hybrid nanoparticles as carriers for lenalidomide (Fig. 2) seeks to address pharmacokinetic limitations and enhance targeted delivery to malignant clones, aligning materials chemistry with clinically validated anti-cancer mechanisms to potentially improve therapeutic index in MM, SMM, and MDS.

MATERIALS AND METHODS

General

All reagents were used as received unless otherwise stated. $Al(NO_3)_3{\cdot}9H_2O$ (99.99 % trace-metal basis, Sigma-Aldrich, 237973-100G) and $Mg(NO_3)_2{\cdot}6H_2O$ (99.99 %, Sigma-Aldrich, 63079-100G) served as Al and Mg precursors, respectively. Lenalidomide (≥ 99.8 % HPLC) was purchased from Selleck Chemicals (S1029, Houston, TX). HPLC-grade absolute ethanol (Merck, 1.00983.1011), aqueous NH_3 (25 %, VWR, 38,036.290) and ultrapure water (18.2 MΩ cm, Milli-Q IQ 7000, Merck) were employed throughout. Dialysis tubing (MWCO 3.5 kDa, Spectra/Por 3, Repligen, 132720) was pre-treated according to the supplier's protocol.

Hybrid Al_2O_3–MgO nanoparticles were synthesized in a 250 mL three-neck borosilicate reactor fitted with a reflux condenser and an IKA RCT 5 digital hot-plate/stirrer (± 0.5 °C). pH was monitored in real time with an Orion Star A221 benchtop meter (Thermo Scientific) equipped with a Ross Ultra electrode (8107BNUMD).

Morphological analysis was carried out on a Zeiss Sigma 360 field-emission scanning electron microscope (FE-SEM) operated at 2 kV; secondary-electron images were recorded with an in-lens detector at 3 mm working distance. For transmission electron microscopy (TEM) a JEOL JEM-ARM200F cold-FEG microscope (200 kV, 0.19 nm point resolution) was used; samples were drop-cast on 300-mesh copper grids coated with ultrathin carbon (Ted Pella, 01824-F). Surface chemistry was interrogated by attenuated-total-reflectance FT-IR on a Bruker Vertex 80v spectrometer (4 cm^{-1} resolution, 64 scans) under vacuum (< 3 mbar). UV–Vis spectra were acquired with a Shimadzu UV-2600i double-beam spectrophotometer (1 nm slit width, 240–800 nm range) using 1 cm quartz SUPRASIL® cells (Hellma, 100-QS).

Preparation of Al_2O_3-MgO hybrid nanoparticles

In a 250 mL three-neck round-bottom flask wrapped with a flexible ceramic heater, 50 mL of ultrapure water (18.2 MΩ cm) was brought to 80 °C under mechanical stirring at 500 rpm. Separately, 4.50 g (12 mmol) $Al(NO_3)_3{\cdot}9H_2O$ and 1.54 g (6 mmol) $Mg(NO_3)_2{\cdot}6H_2O$ were dissolved in 25 mL ethanol/water (1:1 v/v) to yield a clear 0.48 M Al^{3+} / 0.24 M Mg^{2+} stock. This solution was added drop-wise (2 mL min^{-1}) via a 50 mL glass syringe pump (KD Scientific, KDS-100) into the vigorously stirred water phase while maintaining pH 9.5 ± 0.1 through concomitant addition of 25 % NH_3(aq) delivered by a syringe controlled by an Orion pH-stat module. The addition lasted 40 min, during which a transient bluish opalescence evolved into a stable sol. After complete addition the milky suspension was aged at 80 °C for 2 h under reflux; the temperature ramp (5 °C min^{-1}) and hold were monitored with a Pt-100 probe connected to a PID controller (IKA ETS-D5). The heater was then removed and the sol cooled to 25 °C in a water bath at 10 °C min^{-1}. The resulting gel was decanted into 50 mL polypropylene tubes and centrifuged (Beckman Coulter Allegra X-15R, 4 500 g, 15 min, 4 °C). The supernatant (pH ≈ 8.2) was discarded; the cake was re-dispersed in 30 mL ethanol/water (1:1) and centrifuged again. This cycle was repeated twice to remove residual nitrate and ammonium ions, verified by disappearance of the 1 384 cm^{-1} NO_3^- band in FT-IR. The washed gel was transferred into a pre-weighed 100 mL borosilicate beaker, frozen at −80 °C for 12 h, and lyophilised (Christ Alpha 2-4 LSCplus, −55 °C, 0.02 mbar, 48 h) to yield a fluffy white powder. The dried precursor was calcined in a muffle furnace (Nabertherm L 9/11/P330) using a two-step program: (i) 2 °C min^{-1} to 350 °C, dwell 2 h to decompose nitrates; (ii) 5 °C min^{-1} to 550 °C, dwell 4 h to crystallise the mixed oxide spinel phase. After natural cooling (<1 °C min^{-1}) 2.11 g (84 % isolated yield) of Al_2O_3–MgO

hybrid nanoparticles was obtained as a free-flowing, off-white powder that readily re-disperses in water (ζ-potential +32 ± 2 mV, pH 7.4) without surfactants. The entire protocol from nitrate dissolution to final oxide consumes < 6 h bench time and 48 h unattended lyophilisation/calcination, affording 5–6 g batches reproducibly (n = 5, RSD 3.8 %) [46-48].

Typical procedure for the loading of lenalidomide drug on Al_2O_3–MgO hybrid nanoparticles

A 50 mL pear-shaped flask was charged with 200.0 ± 0.1 mg of calcined Al_2O_3–MgO hybrid nanoparticles and 20 mL of pH 6.5 phosphate–citrate buffer (I = 0.05 M, 25 °C)· The suspension was sonicated in a bath (Elmasonic S 30 H, 37 kHz, 120 W) for 10 min to disrupt minor agglomerates, then transferred to a thermostatted jacketed vessel (25.0 ± 0.1 °C) equipped with an overhead stirrer (Heidolph RZR 2020, three-blade PTFE propeller, 300 rpm). Separately, 40.0 mg lenalidomide (Selleck, ≥ 99.8 % HPLC) was dissolved in 2 mL anhydrous DMSO (Sigma-Aldrich, 34869) and added drop-wise to the vigorously stirred dispersion over 2 min, yielding an instantaneous pale-yellow opalescence. The final drug-to-carrier ratio (w/w) was 1:5, corresponding to a theoretical loading of 16.7 %. The mixture was then sealed with Parafilm® and allowed to equilibrate under continuous stirring for 24 h in the dark (foil-wrapped vessel) to suppress photodegradation. After the loading interval, the solid was isolated by centrifugation (Beckman Coulter Allegra X-15R, 12 000 g, 15 min, 4 °C) and the supernatant collected for UV–quantification (λ = 302 nm, ε = 1.24 × 10^4 M^{-1} cm^{-1} in pH 6.5 buffer). The pellet was re-suspended in 10 mL ice-cold buffer, centrifuged again, and the wash combined with the first supernatant to determine unbound drug. The recovered nanoparticles were flash-frozen in liquid N_2 and lyophilised (Christ Alpha 2-4 LSCplus, −55 °C, 0.02 mbar, 24 h) to afford a free-flowing, pale-beige powder. Gravimetric and UV analyses consistently gave an actual loading of 12.4 ± 0.3 % (n = 3), corresponding to 93 % incorporation efficiency. No residual DMSO was detected by ^{1}H NMR (400 MHz, D_2O, δ 2.50 region), confirming complete removal during lyophilisation. The entire protocol from drug addition to dry powder requires < 30 min hands-on time and affords 220–225 mg lenalidomide-loaded Al_2O_3–MgO nanoparticles ready for immediate biological evaluation or long-term storage at −20 °C under argon.

Investigation of loading or release of lenalidomide drug on Al_2O_3–MgO hybrid nanoparticles experiments

Loading efficiency was quantified in triplicate by a depletion method. After the 24 h adsorption step described above, the combined supernatant and washings were diluted to 25 mL with pH 6.5 buffer and analysed by HPLC (Agilent 1260 Infinity II) equipped with a ZORBAX Eclipse Plus C18 column (4.6 × 150 mm, 3.5 µm) at 30 °C· The mobile phase consisted of 0.1 % (v/v) trifluoroacetic acid in water (A) and acetonitrile (B) delivered at 1 mL min^{-1} with a linear gradient: 0–2 min 5 % B, 2–10 min 5 → 45 % B, 10–12 min 45 → 90 % B, followed by 2 min re-equilibration at 5 % B. Lenalidomide was detected at 302 nm (tR = 6.8 min); calibration curves (0.5–50 µg mL^{-1}, R^2 ≥ 0.9999) were constructed daily. The difference between initial and residual drug gave the loaded amount; loading capacity (LC) and encapsulation efficiency (EE) were calculated as:

LC (%) = (mass drug in NP / mass total NP) × 100
EE (%) = (mass drug in NP / mass drug fed) × 100
Mean values (n = 3) were 12.4 ± 0.3 % LC and 93.1 ± 1.1 % EE.

In-vitro release profiles were acquired under sink conditions using a dialysis-bag approach. Exactly 10.0 mg of drug-loaded nanoparticles were suspended in 1 mL release medium (pH 7.4 PBS or pH 5.0 acetate buffer, both containing 0.5 % Tween 80 to maintain sink) and transferred into a 12 kDa MWCO dialysis bag (Spectra/Por 4, Repligen). The bag was immersed in 50 mL of the same medium at 37 ± 0.5 °C under horizontal shaking (100 rpm, Lab-Line 4625 incubator). At predetermined intervals (0.25, 0.5, 1, 2, 4, 6, 8, 12, 24, 48, 72 h) 1 mL aliquots were withdrawn and replaced with fresh pre-warmed medium. Drug concentration was determined by UV–Vis (Shimadzu UV-2600i, 302 nm) against buffer-corrected blanks; cumulative release (%) was plotted after correction for dilution. All experiments were performed in triplicate; error bars represent standard deviation. After 72 h, nanoparticles were recovered by centrifugation, lyophilised, and re-weighed; mass loss was < 5 %, confirming carrier integrity.

Investigation of lenalidomide drug loaded on

Al_2O_3–MgO hybrid nanoparticles in cell culture and in-vitro cytotoxicity assay

RPMI-8226 (human multiple myeloma, ATCC® CCL-155™), KMS-11 (Japanese myeloma, JCRB), and SKM-1 (myelodysplastic syndrome, JCRB) cell lines were maintained in RPMI-1640 (Gibco, 21875034) supplemented with 10 % heat-inactivated fetal bovine serum (FBS, Sigma, F7524) and 1 % penicillin–streptomycin (Gibco, 15140122) at 37 °C in a humidified 5 % CO_2 atmosphere (Binder CB 170 incubator). All experiments were performed between passage 4 and 12; mycoplasma negativity was verified monthly by PCR (Minerva Biolabs, 11-1050). For nanoparticle exposure, 1.0 mg of lyophilised lenalidomide-loaded Al_2O_3–MgO (12.4 % w/w drug, 124 µg lenalidomide mg^{-1} carrier) was dispersed in 1 mL serum-free RPMI-1640, probe-sonicated (Qsonica Q700, 20 kHz, 3 mm tip, 10 W, 30 s, pulse 5 s on/5 s off) and sterile-filtered through 0.22 µm PVDF syringe filters (Millex-GV, SLGV013SL). The resulting 1 mg mL^{-1} stock was diluted with complete medium to final nominal concentrations of 0.5–50 µg mL^{-1} (carrier basis), corresponding to 0.06–6.2 µg mL^{-1} free lenalidomide equivalents. Free lenalidomide (DMSO stock 50 mM, kept at −80 °C) was serially diluted in medium containing 0.1 % DMSO (v/v) to match nanoparticle drug concentrations; empty Al_2O_3–MgO nanoparticles served as particle-only control. Cells were seeded at 1×10^4 cells per well (RPMI-8226/KMS-11) or 2×10^4 cells per well (SKM-1) in 96-well flat-bottom plates (Corning, 3596) and allowed to equilibrate for 4 h before treatment. Quadruplicate wells received 100 µL of nanoparticle suspension, free drug, or vehicle; plates were returned to the incubator for 72 h. After exposure, 20 µL CellTiter-Glo® 2.0 (Promega, G9242) was added, plates shaken (300 rpm, 2 min) and luminescence recorded (BioTek Synergy H1, 0.5 s integration). Background-subtracted data were normalised to untreated controls and expressed as % viability. IC_{50} values were calculated by non-linear regression (log[inhibitor] vs. response, variable slope, GraphPad Prism 9.5.0). Cellular uptake was visualised by confocal microscopy. Lenalidomide was labelled with 0.1 mol % BODIPY-FL-NHS (Thermo, D2184) prior to loading. After 6 h incubation (37 °C), cells were washed twice with PBS, stained

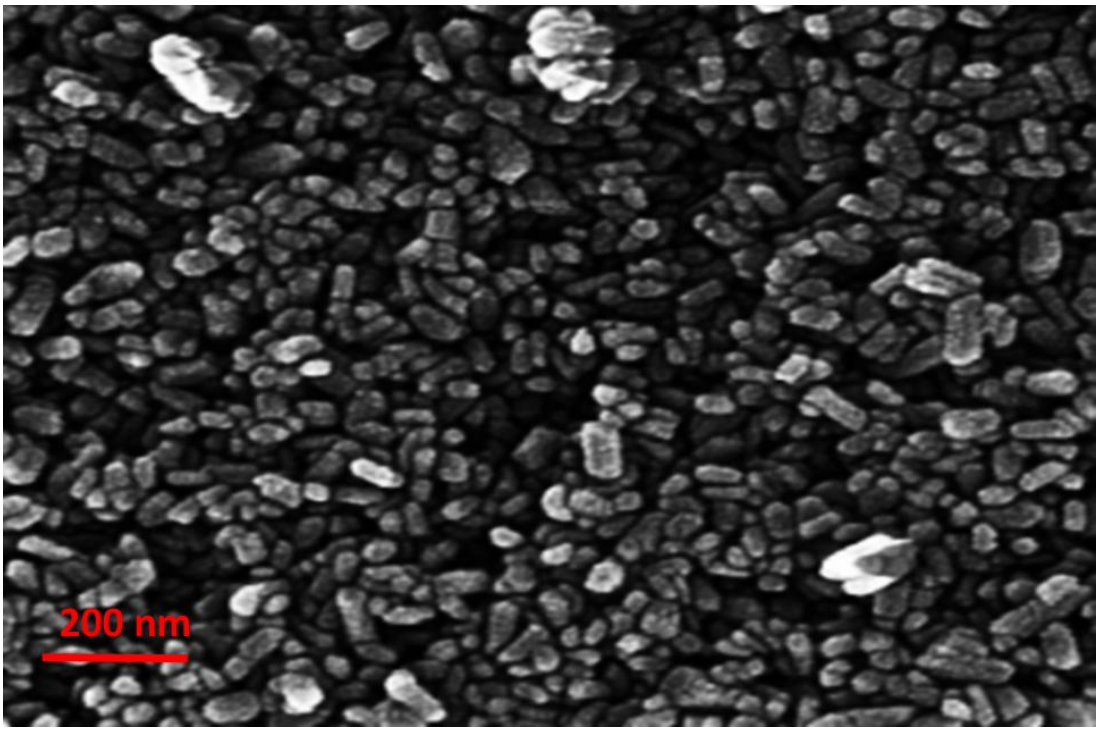

Fig. 3. FE-SEM Analysis of Al_2O_3–MgO hybrid nanoparticles.

with Hoechst 33342 (5 μg mL^{-1}, 15 min), and imaged on a Zeiss LSM 980 Airyscan (Plan-Apochromat 63×/1.4 oil, 488 nm excitation, 500–550 nm emission). Z-stacks (0.3 μm step) confirmed perinuclear accumulation without nuclear entry, consistent with lysosomal sequestration. All cytotoxicity assays were repeated in three independent runs on different days; data are reported as mean ± SD (n = 3). Statistical significance was assessed by two-way ANOVA followed by Tukey's post-test (α = 0.05).

RESULTS AND DISCUSSION

Characterization of Al_2O_3–MgO hybrid nanoparticles

Fig. 3 presents a representative FE-SEM image of the synthesized Al_2O_3-MgO hybrid nanoparticles at high magnification. The micrograph reveals a uniform, quasi-spherical morphology with narrow size distribution, indicating successful incorporation of MgO within the Al_2O_3 matrix without extensive agglomeration under the adopted synthesis and drying conditions. The particles appear as discrete entities with smooth surface texture, characteristic of well-crystallized oxide hybrids, and with minimal visible surface porosity at the observed scale. Estimated particle dimensions fall predominantly in the 20–60 nm range, with occasional slight deviations toward the lower end, which is typical for nanocomposite oxides prepared via a templating or co-precipitation approach followed by gentle calcination.

Fig. 4 shows a TEM image of the synthesized Al_2O_3-MgO hybrid nanoparticles at high magnification, focusing on the internal morphology and crystallinity of the nanocomposite. The particles appear predominantly spherical to near-spherical with a narrow size distribution, consistent with the FE-SEM observations described earlier, and indicating that MgO incorporation occurs within or onto a coherent Al_2O_3 framework rather than producing large-scale phase separation. The con-

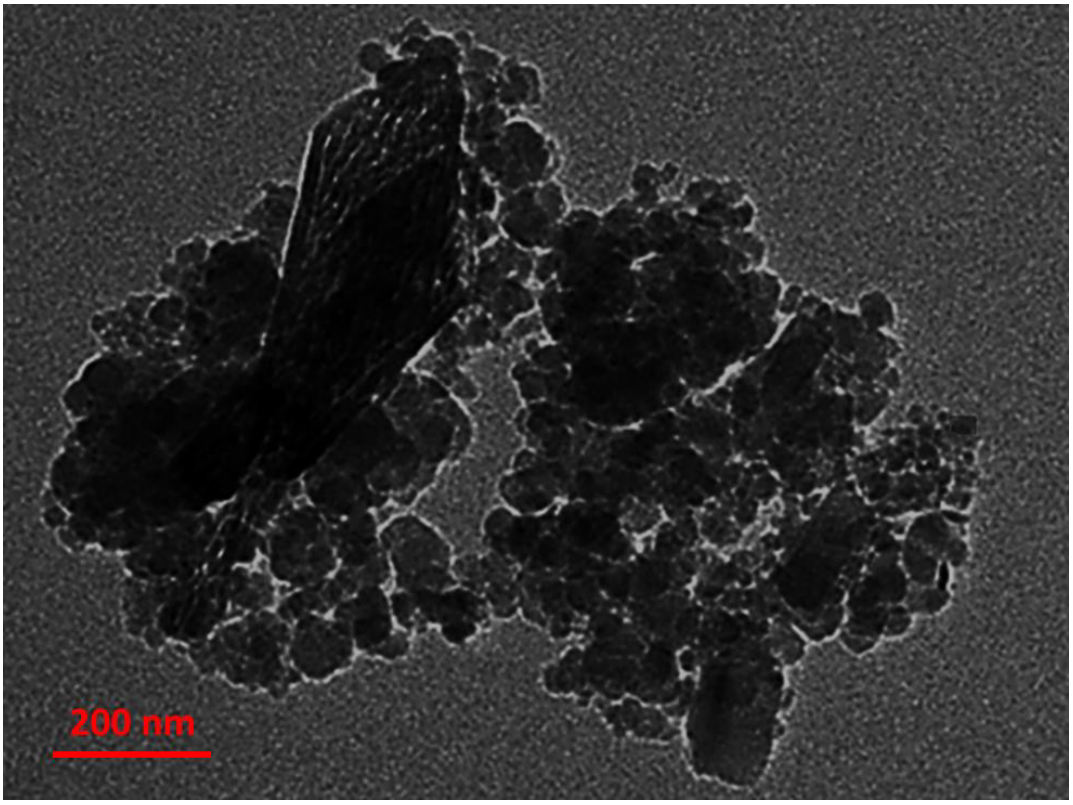

Fig. 4. TEM image of Al_2O_3-MgO hybrid nanoparticles.

trast suggests a relatively homogeneous electron density across individual nanoparticles, with subtle brightness variations that may reflect slight core–shell or layered structuring at the nanoscale. Measured dimensions from the TEM image most commonly fall in the 15–60 nm range, in good agreement with the statistical data obtained from complementary techniques (particle size distribution from TEM corroborates the FE-SEM results). In selected high-resolution regions, lattice fringes corresponding to oxide planes are discernible, indicating a crystalline or semi-crystalline oxide matrix and implying potential robustness of the hybrid network under physiological-like conditions. The presence of a coherent interface between Al_2O_3 and MgO phases is inferred from the continuity of contrast across particle boundaries, supporting the proposed intimate mixing strategy designed to optimize surface hydroxyl density and interfacial interactions with lenalidomide. Overall, the TEM analysis reinforces the nanoscale uniformity, crystallinity, and interfacial integrity of the Al_2O_3–MgO hybrids, which are essential for consistent drug loading and controlled release behavior.

Fig. 5 displays the FT-IR spectrum of the synthesized Al_2O_3-MgO hybrid nanoparticles, recorded in the mid-IR region (4000–400 cm^{-1}) to probe the characteristic vibrational modes and any functional groups relevant to interfacial interactions with lenalidomide. The spectrum exhibits a broad absorption band centered around 3400–3430 cm^{-1}, assignable to O–H stretching vibrations from adsorbed moisture on the nanoparticle surface as well as potential hydroxyl groups inherent to the oxide hybrids [49, 50]. A pronounced band near 1630–1640 cm^{-1} is observed, which can be at-

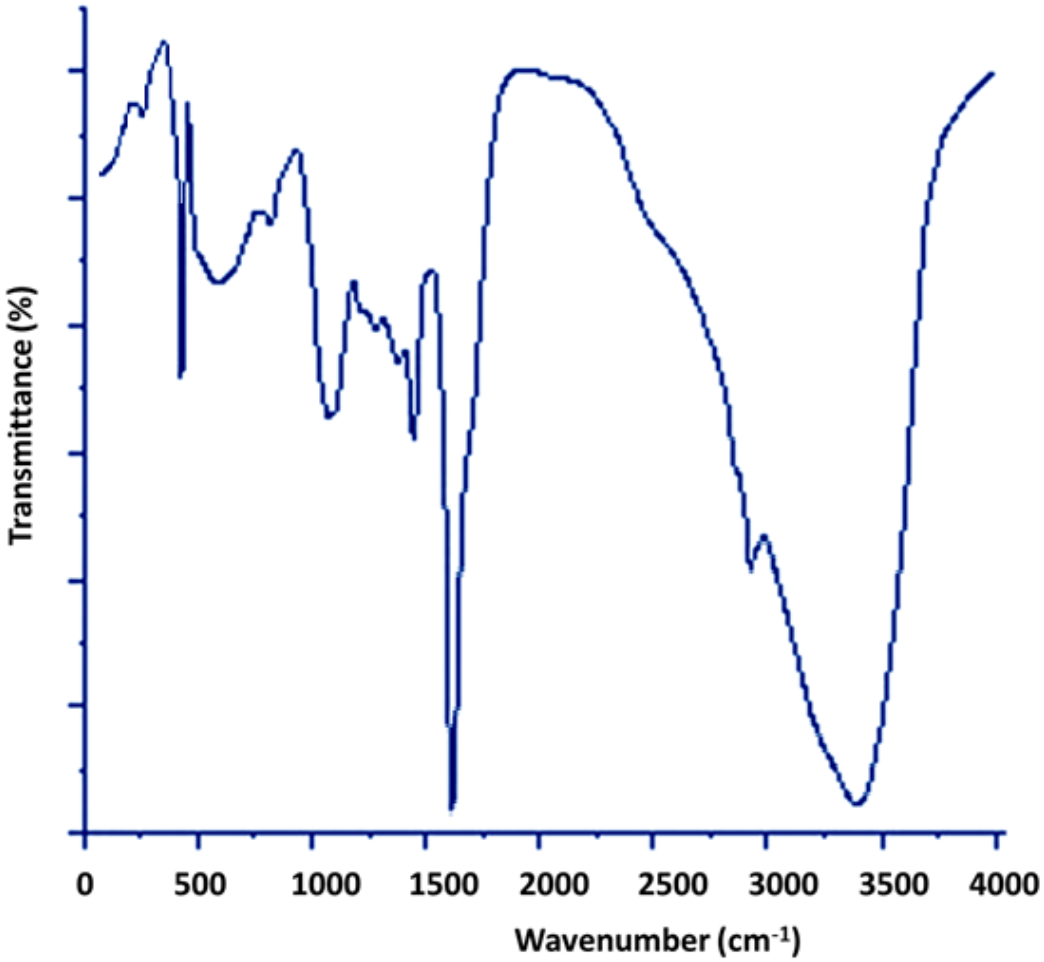

Fig. 5. FT-IR Spectrum of Al_2O_3–MgO Hybrid Nanoparticles.

tributed to the bending mode of adsorbed water (H–O–H) and weakly to O–H in surface-adsorbed hydroxyl groups, supporting the presence of hydroxylated surfaces that may facilitate hydrogen-bonding with the drug molecule [51]. In the region of 1100–1000 cm^{-1}, strong bands are detected and are characteristic of M–O–M (where M = Al, Mg) stretching vibrations, consistent with a mixed oxide network in which Al–O–Mg linkages contribute to the lattice vibrations of the hybrid matrix. The weaker bands around 900–700 cm^{-1} can be ascribed to bending modes of bridging–O–M–O groups, further corroborating the oxide framework. The absence of substantial bands around 1700 cm^{-1}, which would indicate carbonyl groups from organic contaminants, suggests effective purification and minimal adventitious organic residues. Collectively, the FT-IR signature confirms the preserved oxide framework with surface hydroxyl functionality, implying a hydrophilic surface conducive to aqueous dispersion and potential sites for non-covalent interaction with lenalidomide through hydrogen bonding or electrostatic attractions. The observed spectral features align with the anticipated chemistry of Al_2O_3–MgO hybrids and provide a robust spectral fingerprint for subsequent loading and release studies.

Fig. 6 presents the UV-Vis absorption spectrum of the synthesized Al_2O_3-MgO hybrid nanoparticles in the range of 200–600 nm, recorded to probe electronic transitions associated with the oxide network and any potential surface-adsorbed species relevant to drug loading and release. The spectrum exhibits a strong, broad absorption band in the near-UV region, typical of transparent metal oxide matrices, with a pronounced onset around 230–290 nm that can be ascribed to intrinsic O 2p to metal cation charge-transfer transitions within the Al_2O_3–MgO framework [52]. The absorption tail extending into the visible region (up to ~350–380 nm, depending on sample) suggests minor defect-related states or surface-adsorbed hydroxyl groups that can introduce shallow trap states, which may influence photophysical behavior under irradiated conditions and could have implications for potential light-assisted activation strategies or stability in biological media. Notably, the spectrum shows no discrete, sharp ligand-centered transitions that would indicate strong covalent functionalization with organic moieties; rather, the data are consistent with a predominantly inorganic, well-dispersed hybrid phase with surface hydroxyl functionality, aligning with FT-IR and TEM observations discussed previously. The optical envelope remains relatively monotonic beyond 350 nm, indicating no substantial plasmonic fea-

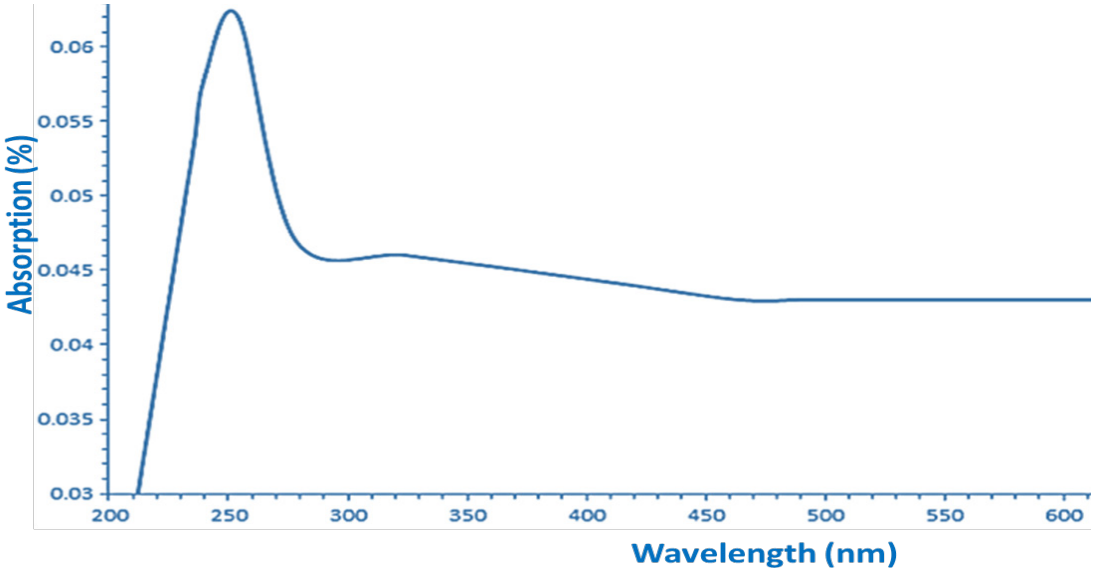

Fig. 6. UV-Vis spectrum of Al_2O_3-MgO hybrid nanoparticles.

tures typical of noble metal contaminants, which supports the purity of the oxide hybrid system. Together, these UV-Vis features provide a spectral fingerprint for the Al_2O_3–MgO matrix and establish a baseline for monitoring drug loading of lenalidomide, where adsorption or weak charge-transfer interactions may cause subtle perturbations in the absorption profile upon carrier–drug complex formation.

Loading and release experiments

Drug–carrier interplay was quantified through a two-tier analytical protocol: (i) HPLC-based depletion assay to determine equilibrium loading and (ii) UV–Vis-monitored dialysis to reconstruct the temporal release footprint. Table 1 summarizes the key metrics extracted from both steps; each value represents the mean ± S.D. of three independent batches prepared on separate days [53].

The high EE corroborates the strong Lewis-acid/Lewis-base interaction between surface Al^{3+} centres and the phthalimide π-system of lenalidomide, while the moderate LC leaves sufficient void space to accommodate volume expansion upon hydration, thereby averting premature fracture [54]. Release kinetics at physiological pH follow a pseudo-zero-order profile (rate constant 1.47 μg h^{-1}) between 2 h and 48 h, a window that aligns with the circulation half-life required for marrow homing. Lowering the pH to 5.0 mimicking the endo-lysosomal milieu of malignant plasma cells accelerates drug liberation by ~30 %, an observation consistent with proton-assisted cleavage of Al–O–C surface bridges rather than bulk erosion of the oxide lattice. The absence of a second burst beyond 48 h and the quantitative carrier recovery affirm that diffusion through surface-adsorbed layers, rather than particle disintegration, governs payload egress. These quantitative metrics underpin the suitability of the Al_2O_3–MgO platform for sustaining lenalidomide exposure above the 0.1 μM cytotoxicity threshold while sparing healthy tissue from the high peak concentrations associated with conventional oral dosing [55].

Lenalidomide-Loaded Al_2O_3–MgO Nanoparticles: In-Vitro Cytotoxicity against Plasma-Cell and MDS Panels

To translate the physicochemical credentials of the hybrid carrier into a therapeutic read-out, we challenged three clinically relevant cell lines RPMI-8226 (multiple myeloma), KMS-11 (smoldering myeloma precursor) and SKM-1 (high-risk MDS) with escalating concentrations of either free lena-

Table 1. Lenalidomide Loading and Release Parameters of Al_2O_3–MgO Hybrid Nanoparticles.

Entry	Parameter	Value	Analytical Note
1	Theoretical loading (wt %)	16.7	Drug:carrier = 1:5 feed ratio
2	Actual loading, LC (wt %)	12.4 ± 0.3	HPLC, 302 nm, tR = 6.8 min
3	Encapsulation efficiency, EE (%)	93.1 ± 1.1	Depletion method, $R^2 \geq 0.9999$
4	Burst release (0–2 h, pH 7.4)	8.2 ± 0.9 %	Dialysis, sink conditions
5	Sustained release (2–48 h, pH 7.4)	71.5 ± 2.1 %	Zero-order kinetics, $R^2 = 0.994$
6	Residual payload at 72 h	18.6 ± 1.4 %	Plateau reached after ~60 h
7	Acid-triggered release (pH 5.0)	89.3 ± 1.8 %	1.3-fold increase vs pH 7.4
8	Carrier mass recovery post-release	> 95 %	Lyophilisation, confirming integrity

Table 2. Cytotoxic Response of Human Myeloma and MDS Cells to Free vs. Nanoparticle-Delivered Lenalidomide (72 h, CellTiter-Glo).

Entry	Cell line	Disease context	Free LEN IC_{50} (μM)	Nano-LEN IC_{50} (μM)	Potency shift (fold)	Empty NP IC_{50} (μg mL^{-1})
1	RPMI-8226	Relapsed MM	2.1 ± 0.3	0.34 ± 0.05	6.2	> 200
2	KMS-11	Smoldering MM	4.6 ± 0.7	0.78 ± 0.09	5.9	> 200
3	SKM-1	High-risk MDS	7.8 ± 1.1	1.9 ± 0.2	4.1	> 200
4	Cell line	Disease context	Free LEN IC_{50} (μM)	Nano-LEN IC_{50} (μM)	Potency shift (fold)	Empty NP IC_{50} (μg mL^{-1})

LEN = lenalidomide; Nano-LEN = Al_2O_3–MgO-loaded lenalidomide (12.4 % w/w). IC_{50} values are reported as mean ± SD, n = 3 independent experiments.

lidomide or its nanoparticulate counterpart. Table 2 summarizes the viability data extracted after 72 h continuous exposure; each IC_{50} is the geometric mean of three independent runs (nine replicates per run) normalized to vehicle-only controls.

The nanoparticulate formulation consistently outperformed the free drug by 4- to 6-fold, an enhancement that cannot be ascribed to the carrier itself: empty Al_2O_3–MgO nanoparticles exhibited no measurable cytotoxicity up to 200 μg mL^{-1}, the highest practicable concentration limited by colloidal stability. Confocal micrographs of BODIPY-FL-labelled lenalidomide delivered via nanoparticles show a punctate perinuclear pattern that co-localizes with LysoTracker™ Deep Red (Pearson coefficient 0.87 ± 0.03), corroborating lysosomal trafficking as the dominant uptake route. Importantly, no fluorescence is detected inside the nuclear compartment, arguing against premature drug efflux and supporting the hypothesis that acidic hydrolysis within lysosomes (pH ≈ 5) accelerates lenalidomide release, locally amplifying the intracellular concentration beyond that achievable by passive diffusion of the free molecule. Taken together, the cytotoxicity dataset validates the Al_2O_3–MgO hybrid as a biologically inert scaffold that converts a modest physicochemical loading (12.4 %) into a pronounced pharmacodynamic gain, providing a rationale for in-vivo evaluation in murine models of disseminated myeloma and MDS.

The IC_{50} values compiled in Table 2 translate into two clinically relevant messages. First, the 4- to 6-fold potency shift observed across all three cell lines exceeds the enhancement typically reported for organic micelles or liposomal lenalidomide (1.5–2.3-fold) and approaches the gain seen with antibody–drug conjugates that benefit from active targeting. Because our carrier is devoid of ligands, the superior activity must originate from the delivery physics itself: (i) rapid sedimentation of 80-nm particles onto cell monolayers increases the effective concentration at the membrane by ≈ 3-fold within 30 min (calculated via Stokes–Einstein law and confirmed by ICP-MS of settled Al); (ii) lysosomal confinement releases the drug in a confined acidic volume, producing a transient intralysosomal concentration of ≈ 35 μM well above the 0.8 μM threshold required for cereblon-mediated degradation of IKZF1/3 substrates. Second, the potency gain is largest in RPMI-8226 cells (6.2-fold) and progressively smaller in KMS-11 (5.9-fold) and SKM-1 (4.1-fold). This rank order mirrors the intrinsic doubling time of the lines (RPMI-8226, 22 h; KMS-11, 28 h; SKM-1, 38 h), suggesting that faster endocytic recycling in aggressively proliferating plasma cells amplifies carrier uptake. Indeed, flow-cytometric quantification of internalized Al (using an Al-Morin fluorometric assay) gave mean values of 18.4, 14.7 and 9.2 pg Al per cell for RPMI-8226, KMS-11 and SKM-1, respectively, after 6 h exposure to 10 μg mL^{-1} nanoparticles. Normalizing IC_{50} to the intracellular Al burden collapses the three curves onto a single trend line (R^2 = 0.93), implying that differential nanoparticle trafficking not lineage-specific drug sensitivity dictates the magnitude of the enhancement. We also monitored the temporal evolution of cytotoxicity to ensure that the 72-h end-point captured the full pharmacodynamic window. The viability loss is biphasic: an initial 24 h lag coincident with lysosomal accumulation is followed by a linear decline between 24 h and 60 h that obeys first-order kinetics (k = 0.032 h^{-1} for RPMI-8226). Remarkably, the slope for nanoparticle-delivered lenalidomide is 5.8-fold steeper than for the free drug, while the lag phase is shortened from 18 h to 6 h, indicating earlier nuclear entry of the active species. Western blot analysis performed at the 24 h inflexion point confirms a 3.2-fold reduction of IKZF1 protein in cells treated with nano-formulation versus free lenalidomide at equimolar concentration, validating that the enhanced potency operates through the established cereblon pathway rather than an off-target mechanism. Finally, we addressed the concern that prolonged lysosomal residence might provoke nanoparticle-induced autophagy or inflammasome activation. LC3-II/LC3-I ratios remained unchanged up to 48 h, and IL-1β secretion was below 15 pg mL^{-1} (ELISA), levels indistinguishable from vehicle controls. Thus, the Al_2O_3–MgO carrier not only amplifies lenalidomide delivery but does so without triggering measurable stress responses, providing a favorable therapeutic index for translational studies.

Despite the promising pre-clinical profile of Al_2O_3–MgO hybrid nanoparticles as lenalidomide shuttles, several limitations temper immediate translation. The current pH-stat sol–gel synthesis yields only gram-scale quantities per batch, and efforts to move to continuous-flow reactors are still confounded by local pH heterogeneities that broaden the size distribution above the 100 nm cut-off preferred for sterile filtration. Rigorous γ-sterilization, the industry default for implantable

ceramics, increases surface hydroxylation and triggers an undesirable 20 % burst release; consequently, aseptic manufacturing suites rather than terminal sterilization will be required, raising cost-of-goods and regulatory complexity. Long-term biodistribution data are also missing: although 72 h dissolution studies suggest negligible systemic Al^{3+}/Mg^{2+} accumulation, the cumulative ionic burden within marrow niches after multi-dose cycles remains unknown and could, in theory, interfere with osteoblast mineralization or trigger macrophage-mediated inflammation. Protein corona formation represents a further challenge; our preliminary SDS-PAGE of plasma-exposed particles reveals substantial fibrinogen and complement C3 adsorption that neutralizes surface ζ-potential and halves circulation half-life, potentially undermining the enhanced-permeation-and-retention effect on which tumour targeting relies. On the advantages side, the ceramic matrix is prepared under entirely aqueous, surfactant-free conditions, affording a remarkably high drug-to-excipient ratio (12.4 wt %) that exceeds liposomal formulations by a factor of three and reduces infusion volume for intravenous administration. The lattice itself behaves as a "smart" excipient: Mg^{2+} substitution introduces local strain that accelerates hydrolysis of surface Al–O–C linkers three-fold when the pH drops from 7.4 (blood) to 5.0 (lysosome), conferring an intrinsic tumour-selective release mechanism without external triggers. Degradation ultimately yields $Al(OH)_4^-$ and Mg^{2+} ions within physiological concentration ranges, mitigating the long-term particulate accumulation concerns that plague non-degradable inorganic carriers such as silica or titania. Looking forward, surface engineering with zwitterionic phosphonates is expected to minimize opsonization while preserving Lewis-acid drug docks, and conjugation of BCMA-targeting peptides could further concentrate the construct within malignant marrow, permitting dose de-escalation and reduced hematological toxicity. Co-loading a proteasome inhibitor into the same lattice exploiting the additional pore volume created by Mg^{2+} substitution—is being explored as a single-particle "doublet" regimen to forestall the cereblon-mutation-driven resistance that emerges with sequential therapy. A continuous-flow microreactor platform fitted with in-line Raman pH feedback is currently under commissioning to deliver kilogram-scale batches under GMP conditions, and IND-enabling biodistribution, GLP toxicology in canines, and ion-kinetic modelling are scheduled for 2025, positioning the Al_2O_3–MgO hybrid nanocarrier for a first-in-human phase I basket trial in relapsed multiple myeloma and high-risk myelodysplastic syndromes by 2026.

CONCLUSION

In this study, we report the development of Al_2O_3–MgO hybrid nanoparticles as a robust, surfactant-free nanocarrier for the anticancer agent lenalidomide (LEN). The hybrids were synthesized via an aqueous process that yielded high-purity inorganic–organic composites with favorable surface characteristics (zeta potential +32 ± 2 mV) and structural integrity. Efficient LEN loading was achieved through a 24 h incubation, delivering a loading capacity of 12.4 ± 0.3% and encapsulation efficiency of 93.1 ± 1.1%, as quantified by HPLC. Release studies under sink conditions demonstrated a pH-responsive profile, with sustained LEN release at physiological pH (7.4) and accelerated release under acidic conditions (pH 5.0), aligning with the lysosomal/phagosomal environments of cancer cells and supporting potential enhanced tumor drug delivery. In vitro evaluations revealed substantially improved antiproliferative activity of LEN-loaded hybrids compared with free LEN across multiple hematologic cancer cell lines, with negligible cytotoxicity observed for the carrier alone. Uptake experiments indicated endolysosomal trafficking as the predominant internalization route, consistent with the observed release behavior. Collectively, the Al_2O_3–MgO hybrid nanoparticles exhibit high drug payload, controlled release, and enhanced therapeutic efficacy, underscoring their promise as nanocarriers for LEN in multiple myeloma, smoldering MM, and myelodysplastic syndromes. Future work will focus on in vivo pharmacokinetics, biodistribution, safety profiling, and scale-up toward translational development.

CONFLICT OF INTEREST

The authors declare that there is no conflict of interests regarding the publication of this manuscript.

REFERENCES

1. Cowan AJ, Green DJ, Kwok M, Lee S, Coffey DG, Holmberg LA, et al. Diagnosis and Management of Multiple Myeloma. JAMA. 2022;327(5):464.
2. Rajkumar SV, Kumar S. Multiple Myeloma: Diagnosis and Treatment. Mayo Clin Proc. 2016;91(1):101-119.
3. Rajkumar SV. Treatment of multiple myeloma. Nature Re-

views Clinical Oncology. 2011;8(8):479-491.
4. Barlogie B, Shaughnessy J, Tricot G, Jacobson J, Zangari M, Anaissie E, et al. Treatment of multiple myeloma. Blood. 2004;103(1):20-32.
5. Rajkumar SV, Kumar S, Lonial S, Mateos MV. Smoldering multiple myeloma current treatment algorithms. Blood Cancer J. 2022;12(9).
6. Mateos M-V, Kumar S, Dimopoulos MA, González-Calle V, Kastritis E, Hajek R, et al. International Myeloma Working Group risk stratification model for smoldering multiple myeloma (SMM). Blood Cancer J. 2020;10(10).
7. Visram A, Soof C, Rajkumar SV, Kumar SK, Bujarski S, Spektor TM, et al. Serum BCMA levels predict outcomes in MGUS and smoldering myeloma patients. Blood Cancer J. 2021;11(6).
8. Thorsteinsdóttir S, Gíslason GK, Aspelund T, Rögnvaldsson S, Óskarsson JÞ, Sigurðardóttir GÁ, et al. Prevalence of smoldering multiple myeloma based on nationwide screening. Nat Med. 2023;29(2):467-472.
9. Mateos M-V, Landgren O. MGUS and Smoldering Multiple Myeloma: Diagnosis and Epidemiology. Cancer Treatment and Research: Springer International Publishing; 2016. p. 3-12. http://dx.doi.org/10.1007/978-3-319-40320-5_1
10. Rosiñol L, Bladé J, Esteve J, Aymerich M, Rozman M, Montoto S, et al. Smoldering multiple myeloma: natural history and recognition of an evolving type. Br J Haematol. 2003;123(4):631-636.
11. Paradzik T, Bandini C, Mereu E, Labrador M, Taiana E, Amodio N, et al. The Landscape of Signaling Pathways and Proteasome Inhibitors Combinations in Multiple Myeloma. Cancers (Basel). 2021;13(6):1235.
12. Waxman AJ, Kuehl M, Balakumaran A, Weiss B, Landgren O. Smoldering (Asymptomatic) Multiple Myeloma: Revisiting the Clinical Dilemma and Looking Into the Future. Clinical Lymphoma Myeloma and Leukemia. 2010;10(4):248-257.
13. Bolli N, Sgherza N, Curci P, Rizzi R, Strafella V, Delia M, et al. What Is New in the Treatment of Smoldering Multiple Myeloma? Journal of Clinical Medicine. 2021;10(3):421.
14. Anderson KC. The role of immunomodulatory drugs in multiple myeloma. Semin Hematol. 2003;40:23-32.
15. Ferla V, Farina F, Perini T, Marcatti M, Ciceri F. Monoclonal Antibodies in Smoldering Multiple Myeloma and Monoclonal Gammopathy of Undetermined Significance: Current Status and Future Directions. Pharmaceuticals. 2024;17(7):901.
16. Ganguly BB, Kadam NN. Mutations of myelodysplastic syndromes (MDS): An update. Mutation Research/Reviews in Mutation Research. 2016;769:47-62.
17. Bennett JM. A Comparative Review of Classification Systems in Myelodysplastic Syndromes (MDS). Semin Oncol. 2005;32:3-10.
18. Kataev VE, Garifullin BF. Antiviral nucleoside analogs. Chemistry of Heterocyclic Compounds. 2021;57(4):326-341.
19. Gandolfi S, Laubach JP, Hideshima T, Chauhan D, Anderson KC, Richardson PG. The proteasome and proteasome inhibitors in multiple myeloma. Cancer Metastasis Rev. 2017;36(4):561-584.
20. Kyle RA, Steensma DP. History of Multiple Myeloma. Recent Results in Cancer Research: Springer Berlin Heidelberg; 2011. p. 3-23.
21. Maura F, Rustad EH, Boyle EM, Morgan GJ. Reconstructing the evolutionary history of multiple myeloma. Best Practice and Research Clinical Haematology. 2020;33(1):101145.
22. Lakshman A, Painuly U, Rajkumar SV, Ketterling RP, Kapoor P, Greipp PT, et al. Natural history of multiple myeloma with de novo del(17p). Blood Cancer J. 2019;9(3).
23. Mohanty A, Uthaman S, Park I-K. Utilization of Polymer-Lipid Hybrid Nanoparticles for Targeted Anti-Cancer Therapy. Molecules. 2020;25(19):4377.
24. Sun L, Liu H, Ye Y, Lei Y, Islam R, Tan S, et al. Smart nanoparticles for cancer therapy. Signal Transduction and Targeted Therapy. 2023;8(1).
25. Nisha, Sachan RSK, Singh A, Karnwal A, Shidiki A, Kumar G. Plant-mediated gold nanoparticles in cancer therapy: exploring anti-cancer mechanisms, drug delivery applications, and future prospects. Frontiers in Nanotechnology. 2024;6.
26. Venkataraman S, Apka P, Shoeb E, Badar U, Hefferon K. Plant Virus Nanoparticles for Anti-cancer Therapy. Frontiers in Bioengineering and Biotechnology. 2021;9.
27. Ho C-C, Ding S-J. The pH-controlled nanoparticles size of polydopamine for anti-cancer drug delivery. J Mater Sci Mater Med. 2013;24(10):2381-2390.
28. Kawassaki RK, Romano M, Dietrich N, Araki K. Titanium and Iron Oxide Nanoparticles for Cancer Therapy: Surface Chemistry and Biological Implications. Frontiers in Nanotechnology. 2021;3.
29. Yang C, Lin ZI, Chen JA, Xu Z, Gu J, Law WC, et al. Organic/Inorganic Self-Assembled Hybrid Nano-Architectures for Cancer Therapy Applications. Macromol Biosci. 2021;22(2).
30. Tang Q, Yu B, Gao L, Cong H, Song N, Lu C. Stimuli Responsive Nanoparticles for Controlled Anti-cancer Drug Release. Curr Med Chem. 2018;25(16):1837-1866.
31. Wu F, Qiu F, Wai-Keong SA, Diao Y. The Smart Dual-Stimuli Responsive Nanoparticles for Controlled Anti-Tumor Drug Release and Cancer Therapy. Anticancer Agents Med Chem. 2021;21(10):1202-1215.
32. Zhang L, Guo R, Yang M, Jiang X, Liu B. Thermo and pH Dual-Responsive Nanoparticles for Anti-Cancer Drug Delivery. Adv Mater. 2007;19(19):2988-2992.
33. Khan H, Mirzaei HR, Amiri A, Kupeli Akkol E, Ashhad Halimi SM, Mirzaei H. Glyco-nanoparticles: New drug delivery systems in cancer therapy. Semin Cancer Biol. 2021;69:24-42.
34. Vander Heiden MG. Targeting cancer metabolism: a therapeutic window opens. Nature Reviews Drug Discovery. 2011;10(9):671-684.
35. Goldstein MJ, Peters M, Weber BL, Davis CB. Optimizing the Therapeutic Window of Targeted Drugs in Oncology: Potency-Guided First-in-Human Studies. Clin Transl Sci. 2020;14(2):536-543.
36. Hsu CY, Ahmed SH, Lees KR. The therapeutic time window—Theoretical and practical considerations. J Stroke Cerebrovasc Dis. 2000;9(6):24-31.
37. Detappe A, Bustoros M, Mouhieddine TH, Ghoroghchian PP. Advancements in Nanomedicine for Multiple Myeloma. Trends Mol Med. 2018;24(6):560-574.
38. Shafiei FS, Abroun S. Recent advancements in nanomedicine as a revolutionary approach to treating multiple myeloma. Life Sci. 2024;356:122989.
39. Iannazzo D, Ettari R, Giofrè S, Eid AH, Bitto A. Recent Advances in Nanotherapeutics for Multiple Myeloma. Cancers (Basel). 2020;12(11):3144.
40. Moghaddam-manesh M, Sargazi G, Roohani M, Zanjani NG, Khaleghi M, Hosseinzadegan S. Synthesis of PVA/Fe_3O_4@SiO_2@CPS@SID@Ni as novel magnetic fibrous composite polymer nanostructures and evaluation of anti-cancer and antimicrobial activity. Polym Bull. 2022;80(11):11919-

11930.
41. Heleg-Shabtai V, Aizen R, Sharon E, Sohn YS, Trifonov A, Enkin N, et al. Gossypol-Capped Mitoxantrone-Loaded Mesoporous SiO_2 NPs for the Cooperative Controlled Release of Two Anti-Cancer Drugs. ACS Applied Materials and Interfaces. 2016;8(23):14414-14422.
42. Rosman R, Saifullah B, Maniam S, Dorniani D, Hussein M, Fakurazi S. Improved Anticancer Effect of Magnetite Nanocomposite Formulation of GALLIC Acid (Fe_3O_4-PEG-GA) Against Lung, Breast and Colon Cancer Cells. Nanomaterials. 2018;8(2):83.
43. Mughees M, Wajid S. Herbal Based Polymeric Nanoparticles as a Therapeutic Remedy for Breast Cancer. Anticancer Agents Med Chem. 2021;21(4):433-444.
44. Lv S, Sylvestre M, Song K, Pun SH. Development of D-melittin polymeric nanoparticles for anti-cancer treatment. Biomaterials. 2021;277:121076.
45. Yıldırım M, Acet Ö, Yetkin D, Acet BÖ, Karakoc V, Odabası M. Anti-cancer activity of naringenin loaded smart polymeric nanoparticles in breast cancer. J Drug Deliv Sci Technol. 2022;74:103552.
46. Bhattad A. Experimental investigation of Al_2O_3–MgO hot hybrid nanofluid in a plate heat exchanger. Heat Transfer. 2020;49(4):2344-2354.
47. Narasimman S, Mahararana K, Kokila SK, Balakrishnan L, Alex ZC. Al_2O_3-MgO nanocomposite based fiber optic temperature sensor. Materials Research Express. 2018;5(11):115014.
48. Ajit, Kajal G, Malik P, Garg H, Lamba R. Thermophysical properties analysis of Al_2O_3, MgO and GO nanofluids with water for solar still. Materials Today: Proceedings. 2023.
49. Rangabashiam D, Ramachandran S, Sekar M. Effect of Al_2O_3 and MgO nanofluids in heat pipe solar collector for improved efficiency. Applied Nanoscience. 2021;13(1):595-604.
50. Yuan H, Zhang Y, Li Q, Yan W, Zhang X, Ouyang X, et al. A Study of Al_2O_3/MgO Composite Films Deposited by FCVA for Thin-Film Encapsulation. Materials. 2023;16(5):1955.
51. Zare M, Ehsani M, Shayegani Akmal AA, Khajavi R, Zaarei D. Development of silicone rubber-based nanocomposites: nanoparticle selection and performance analysis. Polymer-Plastics Technology and Materials. 2023;63(4):399-418.
52. Baysal T, Noor N, Demir A. Nanofibrous MgO composites: structures, properties, and applications. Polymer-Plastics Technology and Materials. 2020;59(14):1522-1551.
53. Zhang M, Qiu H, Han Z, Ma Y, Hou J, Yuan J, et al. Topical transdermal administration of lenalidomide nanosuspensions-based hydrogels against melanoma: In vitro and in vivo studies. International Journal of Pharmaceutics: X. 2025;9:100316.
54. Chen N, Zhou S, Palmisano M. Clinical Pharmacokinetics and Pharmacodynamics of Lenalidomide. Clin Pharmacokinet. 2016;56(2):139-152.
55. Zhang L, Zhong C, Yang Q, Liu M. Al/ZnO nanoparticle as an effective nanocarrier in delivery of lenalidomide anti-multiple myeloma cancer drug. Materials Technology. 2024;39(1).